Electro-chemo-mechanical studies of perovskite-structured mixed ionic-electronic conducting SrSn[subscript 1-x]Fe[subscript x]O[subscript 3-x/2+#] part I: Defect chemistry

Citation: Kim, Chang Sub, Sean R. Bishop, Nicola H. Perry, and Harry L. Tuller. "Electro-Chemo-Mechanical Studies of Perovskite-Structured Mixed Ionic-Electronic Conducting SrSn1-xFexO3-X/2+δ part I: Defect Chemistry." Journal of Electroceramics 38, no. 1 (January 11, 2017): 74–80.

As Published: http://dx.doi.org/10.1007/s10832-017-0064-3

Publisher: Springer US

Persistent URL: http://hdl.handle.net/1721.1/107976

Version: Author's final manuscript: final author's manuscript post peer review, without publisher's formatting or copy editing

Electro-chemo-mechanical Studies of Perovskite-Structured Mixed Ionic-Electronic Conducting $SrSn_{1-x}Fe_xO_{3-x/2+\delta}$ Part I: Defect Chemistry

Chang Sub Kim[1,2], Sean R. Bishop[1,2], Nicola H. Perry[1,3], Harry L. Tuller[1,2]
[1]Department of Materials Science and Engineering, Massachusetts Institute of Technology, Cambridge, MA 02139, USA
[2]Materials Processing Center, Massachusetts Institute of Technology, Cambridge, MA 02139, USA
[3] International Institute for Carbon-Neutral Energy Research (WPI-I^{2}CNER), Kyushu University, Nishi-ku Fukuoka 819-0395, Japan

ABSTRACT

Oxygen nonstoichiometry and the defect chemistry of the $SrSn_{1-x}Fe_xO_{3-x/2+\delta}$ (SSF) system were examined by means of thermogravimetry as a function of oxygen partial pressure in the temperature range of 700-1000 °C and compared against the corresponding mixed ionic-electronic conducting titanate, $SrTi_{1-x}Fe_xO_{3-x/2+\delta}$ (STF) system. The alternate B site host cation, Sn, was selected to replicate and extend the STF studies, given its distinct band structure and higher electron mobility associated with its 5s derived conduction band as compared to the 3d nature of the conduction band in the titanate. Though shifted slightly by the larger size of Sn, the defect equilibria – including the oxygen vacancy concentration – were found to be largely dominated by Fe oxidation state, and thus differed only in a limited way from those in STF. Key thermodynamic parameters for $SrSn_{0.65}Fe_{0.35}O_{2.825+\delta}$ (SSF35) were derived including the reduction enthalpy (4.137 ± 0.175 eV), the high temperature electronic band gap (1.755 ± 0.015 eV) and the anion Frenkel enthalpy (0.350 ± 0.350 eV). The implications these observations have for cathode behavior in solid oxide fuel cells are briefly discussed.

Introduction

The high energy conversion efficiency and fuel flexibility of solid oxide fuel cells (SOFCs) make them attractive alternatives for generating electricity from chemical fuels. Operation at temperatures below traditional SOFC operating temperatures (typically > 800 °C) is expected to aid in improving their start/stop times and reduce long-term thermally driven degradation. Lower temperature operation, however, leads to an increase in cell resistance, commonly dominated by slow surface reaction kinetics at the cathode. Previously, the mixed ionic and electronic conducting (MIEC) perovskite-structured $SrTi_{1-x}Fe_xO_{3-x/2+\delta}$ (STF) materials system was identified as a promising candidate for SOFC cathodes, given its rapid oxygen surface exchange kinetics, due in part to the simultaneous presence of ionic and electronic conductivity (i.e. MIEC) [1]. The exchange kinetics of STF were found to correlate with the minority electron charge density [2], which, in turn is determined by defect formation energetics and band structure, as described below.

STF is a MIEC oxide with predominant p-type behavior at high pO_2 (i.e. cathode conditions), pO_2-independent ionic behavior at intermediate pO_2, and n-type behavior at low pO_2 (i.e. anode conditions) [1]. By varying the ratio of Fe to Ti, one can systematically control both the ionic and electronic conductivities of STF over many orders of magnitude. This aspect was viewed as useful in attempting to better understand the role of these defect species in influencing the surface oxygen exchange kinetics of this model SOFC cathode. The position of the Fermi energy (E_F) relative to the conduction band (E_C) defines the electron charge carrier density (n) in the conduction band and is given by the following expression (for a non-degenerate semiconductor with $E_C - E_F > 3kT$).

$$E_C - E_F = -kTln\left(\frac{n}{N_C}\right) \quad (1)$$

where k is the Boltzmann constant, T is the absolute temperature, and N_C is the effective density of conduction band states. As mentioned above, a strong correlation was found between the magnitude of $E_C - E_F$ and the activation energy (E_a) associated with the oxygen reduction reaction (ORR) represented by the surface exchange coefficient (k_{ex}) as derived from electrochemical impedance spectroscopy measurements [2]. This suggested that the minority carrier density n could be the rate determining species in the ORR in STF under cathodic conditions.

In this work, Ti is replaced by Sn, leading to the analogous $SrSn_{1-x}Fe_xO_{3-x/2+\delta}$ (SSF) system. In SSF, the Sn 5s derived energy band, characterized by high electron mobility [3] in SSF replaces the narrower Ti 3d derived band in STF as the conduction band, and is thus expected to lead to a considerable increase in electron mobility in SSF. While there have been previous studies relating to the crystal structure and electrical properties of SSF [4][5], the experimental conditions under which they were examined were limited, as was the modeling of point defect formation and transport. This paper focuses on the derivation of a defect chemical model for SSF based on examination of oxygen nonstoichiometry as a function of temperature, oxygen partial pressure and Fe fraction based on the results of thermogravimetric measurements. In upcoming publications, we examine 1) the electrical conductivity as a function of the same variables as above and characterize both electronic and ionic contributions to the total conductivity and evaluate how these factors impact the cathodic behavior of SSF and 2) the chemical expansion behavior of SSF, which relates the volume change induced in the lattice due to the introduction or removal of defects associated with oxygen stoichiometry changes.

Theory

The oxygen nonstoichiometry in SSF or STF can be written as $3 - \frac{x}{2} + \delta$, where x is the Fe B-site fraction, with built-in oxygen deficiency of *x/2* due to the difference in valence states between the nominally Fe^{3+} and the Sn^{4+} or Ti^{4+} B-site ions under cathodic operating conditions [6][7]. As a consequence, the insertion of extra oxygen into these normally unoccupied sites is denoted as creating 'interstitials'. This is described in terms of anion Frenkel disorder with the reaction written in Kröger–Vink notation as [6]:

$$O_O^x + V_i^x \leftrightarrow V_O^{\cdot\cdot} + O_i'' \tag{2}$$

where O_O^x is an oxygen on an oxygen site with no charge with respect to the lattice, V_i^x is a charge neutral vacancy on an interstitial site (built-in oxygen deficiency), $V_O^{\cdot\cdot}$ is a vacancy on an oxygen site with two positive charges relative to the lattice, and O_i'' is an oxygen ion on an interstitial site with two negative charges relative to the lattice. Full ionization of the ionic defects is assumed, as is reasonable given the temperature range under study. The equilibrium constant can be written as

$$K'_{af} = \frac{[V_O^{\cdot\cdot}][O_i'']}{[O_O^x][V_i^x]} \tag{3}$$

Provided $[V_O^{\cdot\cdot}]$ and $[O_i'']$ remains small relative to $[O_O^x]$ and $[V_i^x]$, the latter can be assumed to remain approximately constant, and it becomes convenient to introduce a new constant K_{af} given by,

$$K_{af} = K'_{af}[O_O^x][V_i^x] = [V_O^{\cdot\cdot}][O_i''] = K_{af}^0 \, e^{-\frac{H_{af}}{kT}} \tag{4}$$

Intrinsic electron-hole pair generation can be written as:

$$\text{nil} \leftrightarrow e' + h^{\cdot} \tag{5}$$

and the equilibrium constant K_i as

$$K_i = np = N_C N_V e^{-E_g/kT} \tag{6}$$

where n and p are the concentrations of electrons and holes in the conduction and valence bands, respectively, and N_C and N_V are effective density of conduction and valence band states, respectively. Similarly, the oxygen reduction reaction can be described by the following reaction and equilibrium constant, K'_{red}:

$$O_O^x \leftrightarrow V_O^{\cdot\cdot} + 2e' + \frac{1}{2}O_2 \tag{7}$$

$$K'_{red} = \frac{[V_O^{\cdot\cdot}]n^2(pO_2)^{\frac{1}{2}}}{[O_O^x]} \tag{8}$$

As for the anion Frenkel equation above, provided $[V_O^{\cdot\cdot}]$ is much lower in magnitude than $[O_O^x]$, the latter can be treated as a constant, and the defect equations simplified as below.

$$K_{red} = K'_{red}[O_O^x] = K^0_{red} e^{-\frac{H_{red}}{kT}} \tag{9}$$

Equation (8) can then be written as

$$[V_O^{\cdot\cdot}]n^2(pO_2)^{\frac{1}{2}} = K_{red} = [V_O^{\cdot\cdot}]_0 {n_i}^2 ({pO_2}^0)^{\frac{1}{2}} \tag{10}$$

where $[V_O^{\cdot\cdot}]_0$ and n_i are the concentrations of oxygen vacancies and electrons at the oxygen partial pressure ${pO_2}^0$ at which the material is simultaneously stoichiometric and the electron-hole density intrinsic. Therefore, n_i, via equation (6), is given by the following equation.

$$n_i = \sqrt{K_i} \tag{11}$$

Lastly, assuming negligible concentrations of cation vacancies, as in reference [1], charge neutrality gives the following equation:

$$2[V_O^{\cdot\cdot}] + p = 2[O_i''] + n \tag{12}$$

Writing n as a function of other variables from equation (12) and substituting $[O_i'']$ and p as $\frac{K_{af}}{[V_O^{\cdot\cdot}]}$ and $\frac{K_i}{n}$ from equations (4) and (6), respectively,

$$n = 2([V_O^{\cdot\cdot}] - [O_i'']) + p = 2\left([V_O^{\cdot\cdot}] - \frac{K_{af}}{[V_O^{\cdot\cdot}]}\right) + \frac{K_i}{n} \tag{13}$$

From equation (10), one can write the oxygen vacancy concentration as:

$$[V_O^{\cdot\cdot}] = \frac{K_{af}^{\frac{1}{2}} K_i (pO_2^0)^{\frac{1}{2}}}{n^2 pO_2^{\frac{1}{2}}} \quad (14)$$

By solving the quadratic equation (13) for n,

$$n = [V_O^{\cdot\cdot}] - \frac{K_{af}}{[V_O^{\cdot\cdot}]} + \sqrt{(\frac{K_{af}}{[V_O^{\cdot\cdot}]} - [V_O^{\cdot\cdot}])^2 + K_i} \quad (15)$$

Substituting equation (14) into equation (15) and solving for $[V_O^{\cdot\cdot}]$ and *n*, analytical solutions for the defect concentrations as a function of the above thermodynamic parameters can be obtained. The oxygen nonstoichiometry is given by the following equation.

$$\delta = \frac{\frac{K_{af}}{[V_O^{\cdot\cdot}]} - [V_O^{\cdot\cdot}]}{[SSF]} \quad (16)$$

where [*SSF*] is defined as the number of SSF formula units per volume, i.e., $1/V_{\text{unit cell}} = 1.56\times10^{22}$ cm^{-3}

Experimental

SSF solid solutions were prepared by a conventional mixed carbonate/oxide route. Strontium carbonate (Alfa Aesar, 99.99%), tin (IV) oxide (Alfa Aesar, 99.9%), and iron (III) oxide (Alfa Aesar, 99.945%) powders were mixed with the desired Sr/Sn/Fe ratio, ball milled with deionized water and ethanol for six hours, dried, and calcined in air at 1300 °C for six hours. The prepared powders were placed in either a cylindrical or rectangular bar shaped stainless steel die, uniaxially pressed at 20 MPa for two minutes, and then sintered in air at 1500 °C for six hours. The density of the bulk samples was obtained by applying Archimedes' principle. The weights of the samples in air and in water were measured, and the relative density of the bulk samples was calculated to be approximately 97% of theoretical density. The orthorhombically distorted perovskite phase was confirmed by X-ray diffraction (XRD) measurements using a PANalytical X'pert Pro diffractometer (Westborough, MA) in Bragg-Brentano geometry.

The oxygen content of samples was measured *in situ* using thermogravimetric analysis (TGA). SSF bulk samples were broken into small pieces of at most few millimeters in each dimension, and placed in an alumina crucible hanging on one side of a Cahn 2000 microbalance beam from a Pt wire. Oxygen partial pressures were controlled by O_2-N_2 (high pO_2), H_2-H_2O-N_2 (low pO_2), and CO-CO_2 (intermediate pO_2) gas mixtures using MKS Instruments 1179A and M100B mass flow controllers (MFCs) (Andover, MA). The oxygen pressure was monitored using an *in situ* Nernst based yttria-stabilized zirconia sensor.

Results

The XRD spectra of $SrSn_{1-x}Fe_xO_{3-x/2+\delta}$ (x = 0, 0.05, 0.35, 0.50) powders are shown in Figure 1, where the notation SSFX represents SSF with x mol% of Fe times 100. All three compositions are consistent with the orthorhombic (close to tetragonal) perovskite phase. All peaks shift toward the right with increasing x, indicating a smaller lattice constant, consistent with the smaller ionic radius of Fe (0.645 Å and 0.585 Å for high spin Fe^{3+} and Fe^{4+} VI-fold coordination, respectively) compared to Sn^{4+} (0.69 Å, VI-fold coordination) [8]. Lattice parameters of SSF were calculated by Rietveld refinement of the XRD spectra and are listed in Table 1. It is also worth noting that the formation of oxygen vacancies induced by Fe doping may also lead to a change in lattice parameter, though typically to a much lower extent than the effect from cation substitution [9].

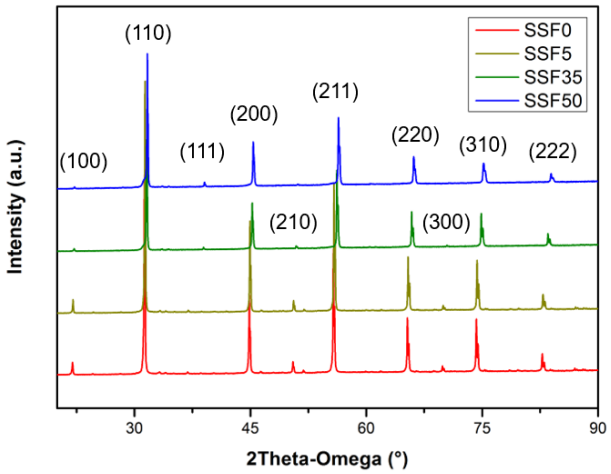

Figure 1. XRD pattern of SSF (x = 0, 0.05, 0.35, 0.50) powders after calcination.

Table 1. Lattice parameters of SSF (x = 0, 0.05, 0.35, 0.50) calculated from XRD patterns and of STF50

	a (Å)	b (Å)	c (Å)
SSF0	5.704637	8.067753	5.704075
SSF5	5.700972	8.062951	5.701623
SSF35	5.667429	8.011297	5.668173
SSF50	5.644334	7.97353	5.64925
STF50 [10]	3.8852	3.8852	3.8852

The oxygen nonstoichiometry (δ) in SSF35, measured by TGA, as a function of pO_2 over the temperature range of 800 - 1000 °C is plotted in Figure 2. In oxidizing conditions (high pO_2), SSF35 absorbs oxygen from the gas phase with increasing pO_2, increasing δ; conversely, as pO_2 decreases, δ decreases. At intermediate pO_2, δ reaches a near constant value. In this region, Fe is in its preferred valence state of 3+. From the charge neutrality condition, this requires that for every two Fe^{3+} cations, one oxygen vacancy is created. Since the oxygen content per formula unit can be written as $3 - \frac{x}{2} + \delta$, where x is the Fe dopant concentration, in this region, $\delta \approx 0$. As expected SSF exhibits increasing levels of reduction with increasing temperature at a given value of pO_2.

In Figure 3, δ vs log pO_2 data for SSF35 is overlayed with that of STF35 [6] for temperatures of 700 and 1000 °C. One observes in oxidizing conditions that SSF35 shows a much lower oxygen excess than STF35 at 700 °C, but the difference becomes smaller at 1000 °C, resulting from the shift in onset of oxidation to higher pO_2. Under reducing conditions, STF35 and SSF35 show nearly identical oxygen nonstoichiometry at 700 °C, but as temperature increases, the onset of reduction for SSF35 shifts to a higher pO_2 than for STF.

The lower Fe containing sample, SSF5 exhibited no measureable change in nonstoichiometry under both intermediate and high pO_2. Under reducing conditions, an irreversible phase transition occurred, confirmed by XRD, and the original mass could not be recovered after reoxidation. The very long time to reach equilibrium (days) under very reducing conditions in the TGA, as compared to the relatively rapid response of SSF35 (hours), served as an indication of the phase change during TGA measurements.

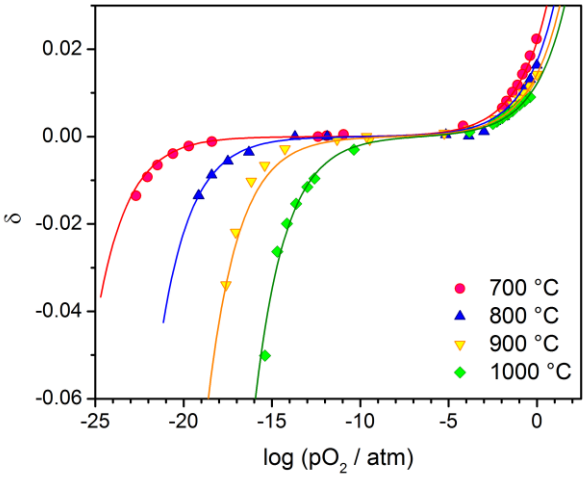

Figure 2. Oxygen nonstoichiometry (δ) as a function of pO_2 and temperature for SSF35.

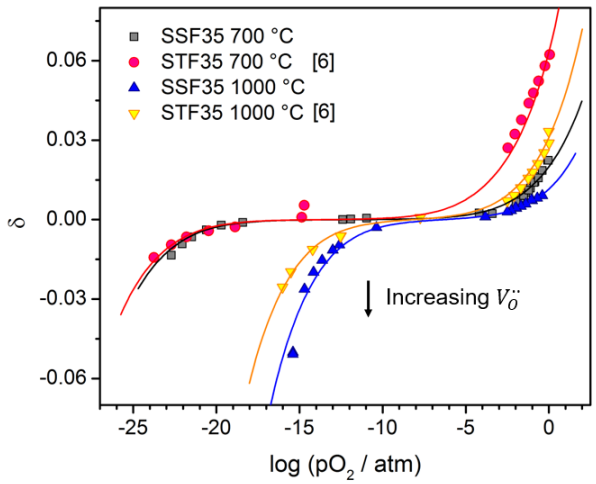

Figure 3. Comparison of oxygen nonstoichiometry of STF35 from [6] and SSF35 at 700 °C and 1000 °C.

Discussion

The TGA results can be divided into different pO_2 regimes, with a subset of each defect species dominating in each regime. This allows one to simplify the electroneutrality equation, equation ((12)), a practice commonly referred to as the Brouwer approximation, such that only one defect species on either side of the equality equation need be considered in a given pO_2 range. For example, at low pO_2, n and $[V_O^{\cdot\cdot}]$ will be much greater in concentrations than p and $[O_i'']$, such that $n \approx 2[V_O^{\cdot\cdot}]$. For the model systems SSF and STF, three different pO_2 regimes, and corresponding approximations, can be obtained, as shown in Figure 4. With the three key defect reactions – anion Frenkel disorder, intrinsic electron-hole pair generation, oxygen reduction – plus the electroneutrality equation, one can obtain analytical solutions for each defect species along with their pO_2 dependences, as shown in Table 2. A schematic defect diagram for the SSF or STF model systems based on these solutions is shown in Figure 4.

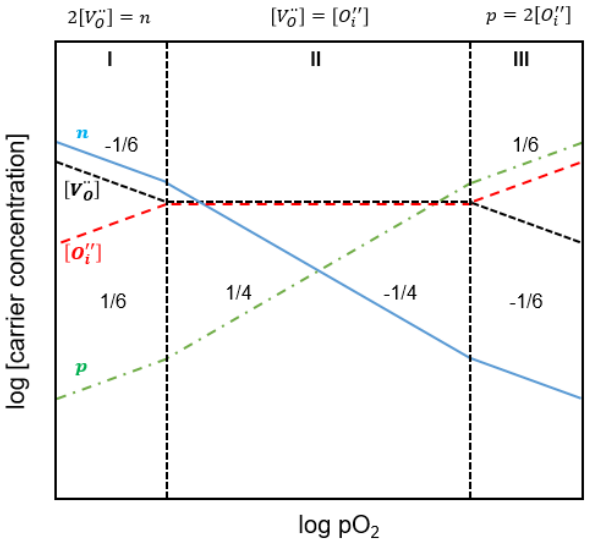

Figure 4. Schematic defect diagram using Brouwer approximation for the model system SSF and STF.

Table 2. The predicted solutions to the defect solutions with Brouwer approximations.

	I	II	III
n	$(2K_{red})^{\frac{1}{3}}\, pO_2{}^{-\frac{1}{6}}$	$\frac{K_{red}{}^{\frac{1}{2}}}{K_{af}{}^{\frac{1}{4}}}\, pO_2{}^{-\frac{1}{4}}$	$\left(\frac{K_i K_{red}}{2K_{af}}\right)^{\frac{1}{3}} pO_2{}^{-\frac{1}{6}}$
p	$\frac{K_i}{(2K_{red})^{\frac{1}{3}}}\, pO_2{}^{\frac{1}{6}}$	$\frac{K_i K_{af}{}^{\frac{1}{4}}}{K_{red}{}^{\frac{1}{2}}}\, pO_2{}^{\frac{1}{4}}$	$\left(\frac{2K_{af}K_i{}^2}{K_{red}}\right)^{\frac{1}{3}} pO_2{}^{\frac{1}{6}}$
$[V_O^{\cdot\cdot}]$	$\left(\frac{1}{4}K_{red}\right)^{\frac{1}{3}} pO_2{}^{-\frac{1}{6}}$	$K_{af}{}^{\frac{1}{2}}$	$\left(\frac{4K_{af}{}^2 K_{red}}{K_i{}^2}\right)^{\frac{1}{3}} pO_2{}^{-\frac{1}{6}}$
$[O_i'']$	$\frac{K_{af}}{\left(\frac{1}{4}K_{red}\right)^{\frac{1}{3}}}\, pO_2{}^{\frac{1}{6}}$	$K_{af}{}^{\frac{1}{2}}$	$\left(\frac{K_{af}K_i{}^2}{4K_{red}}\right)^{\frac{1}{3}} pO_2{}^{\frac{1}{6}}$

The defect equilibrium diagram in Figure 4 presents a wide range of pO_2 over which trends in defect concentration can be visualized. Only a smaller range of defect concentrations are typically accessible with conventional experimental techniques. Figure 5 below shows the results of fitting the defect model described in the theory section to the TGA data shown in Figure 2 above, with the pO_2 range limited to the range of experimental values used in Figure 2. Clearly, similarities exist between the Brouwer diagram in Figure 4 and the experimentally derived defect equilibrium diagram with Figure 5 dominated largely by region II. In this intermediate regime, the oxygen vacancy and interstitial concentrations are approximately constant, while a -1/4 and +1/4 power law dependence is observed for the electron and hole concentrations, respectively. At low pO_2, the oxygen vacancy concentration

dependence changes gradually (as opposed to the abrupt change intrinsic to the approximations shown in the Brouwer approach), from pO_2 independence towards the -1/6 power law dependence expected in Region I of Figure 4. Conversely, at high pO_2, the interstitial content begins to increase with increasing pO_2, but the 1/6 power law is not reached in the experimentally accessible regime.

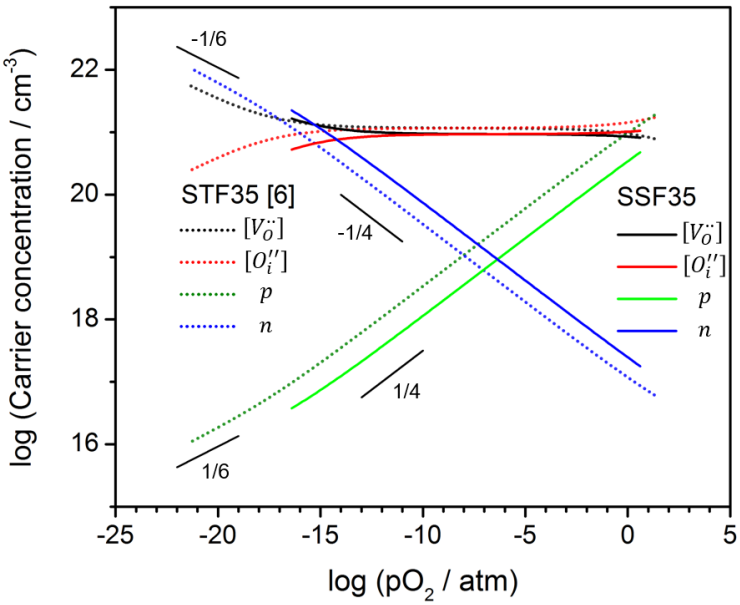

Figure 5. Carrier concentrations from defect equilibria at 1000 °C.

The equilibrium constants, defined in equations (4), (6) and (9), are derived from fitting an analytical solution of equation (14) to the non-stoichiometry data. From the slopes, the thermal band gap and the enthalpies of the anion Frenkel and oxygen reduction reactions are calculated, and reported in Table 3.

A larger band gap was obtained for SSF35 (E_g = 1.755 eV) as compared to STF35 (E_g = 1.379 eV), consistent with the wider plateau observed for SSF35 than for STF35 in Figure 3 at, for example, 700 °C [6]. The larger lattice parameter of SSF implies increased spacing between Fe cations, leading to an expected decrease in wavefunction overlap and thereby band width. This would lead to the observed larger energy gap, arising between the lower lying Fe (3+/4+) and higher lying Fe (2+/3+) 3d orbitals. The enthalpies of anion Frenkel pair generation for SSF35 and STF35 are very similar at about 0.5 eV, as are the reduction enthalpies of about 4 eV. Due to significant cross-sensitivity between the anion Frenkel equilibrium constants and other derived energetic terms, the error bars are large. We also present an alternative fitting model in the appendix that comes to the same conclusion.

Table 3. Thermodynamic parameters for SSF35, compared with STF35 [6], from fitting the nonstoichiometry (δ) as a function of oxygen partial pressure at different temperatures.

	SSF35	STF35 [6]
ΔH_{af} (eV)	0.350 ± 0.350	0.518 ± 0.025
E_g (eV)	1.755 ± 0.015	1.379 ± 0.029
ΔH_{red} (eV)	4.137 ± 0.175	3.893 ± 0.040

Activation energies related to *electron* (1.961±0.051 eV) and *hole* (-0.217±0.006 eV) generation were extracted from the defect equilibrium model over the temperature range 700~1000 °C. From Table 1, the activation energy related to electron generation is given by $\frac{H_{red}}{2} - \frac{H_{af}}{4}$ in the intermediate pO_2 region. Taking into account the derived values for $H_{red} = 4.137 \pm 0.175\ eV$, and $H_{af} = 0.350 \pm 0.350\ eV$, one calculates a value for $E_{a,n} = 1.981 \pm 0.175\ eV$, which agrees well with the above value extracted directly from the defect model.

Similarly, the activation energy related to hole generation at intermediate pO_2 is given by $E_g + \frac{H_{af}}{4} - \frac{H_{red}}{2}$. Taking into account the derived values for H_{red}, H_{af}, and E_g, one calculates a value for $E_{a,p} = -0.226 \pm 0.190\ eV$. This value also agrees well with the value extracted from the defect model, (-0.217±0.006 eV) but with considerably larger uncertainty given the additivity of errors coming from the three thermodynamic parameters.

Lastly, we compare the relative stability of SSF5 and SSF35 versus STF35. As mentioned above, SSF5 was found to decompose under much milder reducing conditions than the other two materials. This suggests that Sn is more susceptible to reduction than Ti and as long as there is sufficient Fe in solid solution to accommodate changes in oxidation state, then the stannate can be stabilized to lower pO_2.

Despite the substitution of Ti with Sn, SSF shows surprisingly similar defect chemistry as compared to the STF counterpart. The defect behavior thus appears to be largely governed by reduction and oxidation of Fe. Subtle differences do exist, such as the larger bandgap energy in SSF, likely due to a lower degree of hybridization between Sn 5s and Fe 3d orbitals, as compared to a larger overlap between Ti 3d and Fe 3d orbitals. From this study, we do not expect any major differences in electrochemical behavior between SSF35 and STF35 to arise based on differences in oxygen defect concentrations. However, differences in Fe hybridization with Ti vs. Sn are expected to alter electrical properties, with this being the subject of a subsequent publication. Additionally, the chemo-mechanical coupling properties, i.e., chemical expansion, of SSF are also under investigation.

Conclusion

The defect equilibria of a new SOFC model cathode material, $SrSn_{1-x}Fe_xO_{3-x/2+\delta}$ have been explored in this study. Key thermodynamic parameters were derived, namely the enthalpy of reduction (4.137 ± 0.175 eV) and electronic band gap (1.755 ± 0.015 eV). The overall trend of oxygen non-stoichiometry data and defect chemistry of SSF was found to be surprisingly similar to that of STF, as reducibility of Fe in the Sr-based perovskite oxide seems to govern the key reactions in both, with the only major difference being the slightly larger lattice parameter of SSF and reduced B-site cation hybridization.

The magnitude of oxygen non-stoichiometry (δ) in SSF was different from that of STF, largely under oxidizing conditions at the lower temperatures of this study for which the regime of oxygen excess was shifted to higher pO_2. This could be attributed to its higher band gap energy related to reduced Sn-Fe hybridization, as compared to Ti-Fe. SSF5 showed low chemical stability under reducing conditions. In order to be used as an electrode for a reversible SOFC, stability in both oxidizing and reducing conditions must be fulfilled, and thus a sufficient Fe concentration as in SSF35 is required for SSF to serve as a potential electrode. In the end, similarities in defect chemistry of STF and SSF suggest comparable electronic and ionic characteristics of the two materials, to be addressed in following work.

Acknowledgement

This publication is based on work funded by the Skolkovo Institute of Science and Technology (Skoltech) through the "Center for Research, Education and Innovation for Electrochemical Energy Storage" under contract number 186-MRA. Partial support from the National Science Foundation under award number DMR-1507047 is also acknowledged. Structural characterization of the materials was conducted in the MRSEC Shared Experimental Facilities at MIT, supported by the National Science

Foundation under award number DMR-1419807. CSK acknowledges S. Cook for valuable discussions on curve fitting. NHP acknowledges support from I2CNER, funded by the World Premier International Research Center Initiative (WPI), MEXT, Japan.

Appendix

Given that the predicted values of nonstoichiometry δ were rather insensitive to the equilibrium constant for anion Frenkel disorder, we followed an alternative approach by setting H_{af} and K_{af}^{0} for SSF35 equal to that of STF35 in reference [6]. For this routine, data points from all temperatures were fit simultaneously by setting enthalpies and pre-exponential terms as variables, instead of fitting equilibrium constants at each temperature. The resulting enthalpies and pre-exponentials are shown in Table 4. Note that H_{red} for both fitting procedures (Table 3 and Table 4) were almost identical (within the error of the value from Table 3), and E_g was less than 3% different, indicating insensitivity to the anion Frenkel disorder energetics.

Table 4. Thermodynamic parameters for STF35 and SSF35 from fitting nonstoichiometry – δ – data as functions of oxygen partial pressure over a range of temperatures simultaneously.

	SSF35	STF35 (refit from data [6])
ΔH_{af} (eV)	0.518 *	0.518 *
K_{af}^{0} (cm^{-6})	1.161×10^{43} *	$(1.161 \pm 0.001) \times 10^{43}$
E_g (eV)	1.710 ± 0.001	1.287 ± 0.001
$N_C N_V$ (cm^{-6})	$(6.433 \pm 0.001) \times 10^{44}$	$(1.861 \pm 0.001) \times 10^{43}$
ΔH_{red} (eV)	4.302 ± 0.001	3.758 ± 0.001
K_{red}^{0} ($cm^{-9} \cdot atm^{\frac{1}{2}}$)	$(2.592 \pm 0.001) \times 10^{72}$	$(2.906 \pm 0.001) \times 10^{69}$

* these values are fixed

References

[1] A. Rothschild, W. Menesklou, H. L. Tuller, and E. Ivers-Tiffée, "Electronic Structure, Defect Chemistry, and Transport Properties of $SrTi_{1-x}Fe_xO_{3-y}$ Solid Solutions," *Chem. Mater.*, vol. 18, no. 16, pp. 3651–3659, 2006.

[2] W. Jung and H. L. Tuller, "A New Model Describing Solid Oxide Fuel Cell Cathode Kinetics: Model Thin Film $SrTi_{1-x}Fe_xO_{3-\delta}$ Mixed Conducting Oxides–a Case Study," *Adv. Energy Mater.*, vol. 1, pp. 1184–1191, 2011.

[3] J. Januschewsky, M. Ahrens, A. Opitz, F. Kubel, and J. Fleig, "Optimized $La_{0.6}Sr_{0.4}CoO_{3-\delta}$ Thin-Film Electrodes with Extremely Fast Oxygen-Reduction Kinetics," *Adv. Funct. Mater.*, vol. 19, no. 19, pp. 3151–3156, 2009.

[4] V. Thangadurai, P. Schmid Beurmann, and W. Weppner, "Mixed oxide ion and electronic conductivity in perovskite-type $SrSnO_3$ by Fe substitution," *Mater. Sci. Eng. B*, vol. 100, no. 1, pp. 18–22, 2003.

[5] V. Thangadurai, R. A. Huggins, and W. Weppner, "Use of simple ac technique to determine the ionic and electronic conductivities in pure and Fe-substituted $SrSnO_3$ perovskites," *J. Power Sources*, vol. 108, no. 1–2, pp. 64–69, 2002.

[6] M. Kuhn, J. J. Kim, S. R. Bishop, and H. L. Tuller, "Oxygen Nonstoichiometry and Defect Chemistry of Perovskite-Structured $Ba_xSr_{1-x}Ti_{1-y}Fe_yO_{3-y/2+\delta}$ Solid Solutions," *Chem. Mater.*, vol. 25, no. 15, pp. 2970–2975, 2013.

[7] K. S. Roh, K. H. Ryu, and C. H. Yo, "Nonstoichiometry and Physical Properties of the $SrSn_{1-x}Fe_xO_{3-y}$System," *J. Solid State Chem.*, vol. 142, no. 2, pp. 288–293, 1999.

[8] R. D. Shannon, "Revised effective ionic radii and systematic studies of interatomic distances in halides and chalcogenides," *Acta Crystallogr. Sect. A*, vol. 32, no. 5, pp. 751–767, 1976.

[9] N. H. Perry, J. J. Kim, S. R. Bishop, and H. L. Tuller, "Strongly coupled thermal and chemical expansion in the perovskite oxide system $Sr(Ti,Fe)O_{3-a}$," *J. Mater. Chem. A*, vol. 3, no. 7, pp. 3602–3611, 2015.

[10] P. Adler and S. Eriksson, "Structural Properties, Mössbauer Spectra, and Magnetism of Perovskite-Type Oxides $SrFe_{1-x}Ti_xO_{3-y}$," *Zeitschrift für Anorg. und Allg. Chemie*, vol. 626, no. 1, pp. 118–124, 2000.